ACS APPLIED MATERIALS & INTERFACES

Research Article

Cite This: ACS Appl. Mater. Interfaces 2018, 10, 26841−26850

www.acsami.org

Interaction of Positively Charged Gold Nanoparticles with Cancer Cells Monitored by an in Situ Label-Free Optical Biosensor and Transmission Electron Microscopy

Beatrix Peter,[†] Istvan Lagzi,[‡,§] Satoshi Teraji,[∥] Hideyuki Nakanishi,[∥] Laszlo Cervenak,[⊥,#] Dániel Zámbó,[¶] András Deák,[¶] Kinga Molnár,[▽] Monika Truszka,[▽] Inna Szekacs,[†] and Robert Horvath*[,†]

[†]Nanobiosensorics Group, Institute of Technical Physics and Materials Science, Centre for Energy Research and [¶]Chemical Nanostructures Group, Institute of Technical Physics and Materials Science, Centre for Energy Research, Hungarian Academy of Sciences, Konkoly-Thege út 29-33, H-1120 Budapest, Hungary

[‡]Department of Physics, Budapest University of Technology and Economics, Budafoki út 8, Budapest H-1111, Hungary

[§]MTA-BME Condensed Matter Research Group, Budafoki út 8, Budapest H-1111, Hungary

[∥]Department of Macromolecular Science and Engineering, Graduate School of Science and Technology, Kyoto Institute of Technology, Matsugasaki, Kyoto 606-8585, Japan

[⊥]Research Laboratory, 3rd Department of Medicine, Semmelweis University, H-1085 Budapest, Hungary

[#]Research Group of Immunology and Hematology, Hungarian Academy of Science, Kútvölgyi út 4., H-1125 Budapest, Hungary

[▽]Department of Anatomy, Cell and Developmental Biology, Eötvös Loránd University, Pázmány Péter stny. 1/C, H-1117 Budapest, Hungary

Supporting Information

ABSTRACT: Functionalized nanoparticles (NPs) can penetrate into living cells and vesicles, opening up an extensive range of novel directions. For example, NPs are intensively employed in targeted drug delivery and biomedical imaging. However, the real-time kinetics and dynamics of NP−living cell interactions remained uncovered. In this study, we in situ monitored the cellular uptake of gold NPs—functionalized with positively charged alkaline thiol—into surface-adhered cancer cells, by using a high-throughput label-free optical biosensor employing resonant waveguide gratings. The characteristic kinetic curves upon NP exposure of cell-coated biosensor surfaces were recorded and compared to the kinetics of NP adsorption onto bare sensor surfaces. We demonstrated that from the above kinetic information, one can conclude about the interactions between the living cells and the NPs. Real-time biosensor data suggested the cellular uptake of the functionalized NPs by an active process. It was found that positively charged particles penetrate into the cells more effectively than negatively charged control particles, and the optimal size for the cellular uptake of the positively charged particles is around 5 nm. These conclusions were obtained in a cost-effective, fast, and high-throughput manner. The fate of the NPs was further revealed by electron microscopy on NP-exposed and subsequently fixed cells, well confirming the results obtained by the biosensor. Moreover, an ultrastructural study demonstrated the involvement of the endosomal−lysosomal system in the uptake of functionalized NPs and suggested the type of the internalization pathway.

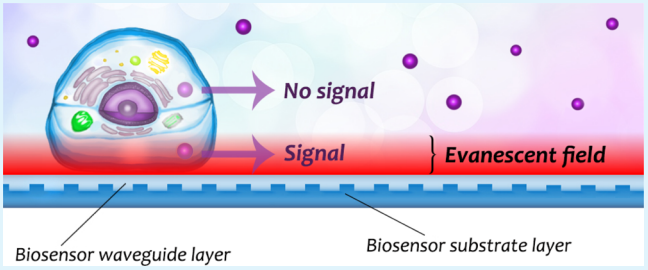

KEYWORDS: *label-free, optical biosensor, positively charged gold nanoparticles, cells, penetration, nanoparticle uptake, adsorption*

INTRODUCTION

Functionalized nanoparticles (NPs) may serve as carriers in targeted drug delivery applications.[1,2] The penetration of NPs into lipid bilayers and cell membranes has significant implications for phototherapy treatments, medical imaging, and NP-actuated vesicles for controlled drug release as well.[3−9] NPs can improve the solubility and stability of active substances, increase their uptake, defend them from early damage in the living systems, and elongate their circulation time.[1,10] They provide high differential uptake efficiency in the target cells over normal ones.[1,10] In this way, NP interference with a biological system may specify its targeting impacts and therapeutic efficacy.[1,11] It has been demonstrated that gold NPs (AuNPs) functionalized with mixed monolayers can

Received: January 27, 2018
Accepted: July 19, 2018
Published: July 19, 2018

DOI: 10.1021/acsami.8b01546
ACS Appl. Mater. Interfaces 2018, 10, 26841−26850

penetrate into living cells[12] and artificial vesicles.[3] However, the real-time kinetics and dynamics of the processes have remained predominantly uncovered. There is a clear need for fast, real-time, cost-effective, and high-throughput platforms to monitor NP−living cell interactions.

There are a variety of techniques to measure and visualize the cellular uptake of metal or other NPs by cells. Inductively coupled plasma mass spectrometry (ICP−MS) and ICP atomic emission spectroscopy are widely used to quantify the number of penetrated NPs inside the cells with outstanding sensitivities.[13−22] Other methods can be applied to visualize them; for example, fluorescence and dark field microscopies, differential interference contrast microscopy, confocal microscopy, surface-enhanced Raman spectroscopy, and, probably the most popular, transmission electron microscopy (TEM).[13−15,23−27] Further techniques have also been used in previous studies for quantifying the uptake, including fluorometry,[28] the fluorescent absorption method and the P2T method,[29] magnetophoresis, and electron spin resonance.[26] The drawbacks of these methods are that they require a large number of cells, the processes and preparations are time-consuming, and, most importantly, these end-point detection techniques do not give information on the kinetics and dynamics of the cellular uptake.[30,31] Recently, the scientific community has turned to label-free biosensors and techniques (capacitance-based sensors, magnetoimpedance biosensors, and on-chip impedance sensors) to monitor the cellular uptake of NPs in a real-time way.[25,30,31]

In the present work, we exploit an evanescent field-based optical biosensor to follow the cellular uptake of positively charged NPs. According to the previous findings,[12] we chose positively charged AuNPs with a diameter of ∼5 nm because of their optimal size and charge for penetration into the cells. The principle of the evanescent-field-based detection is illustrated in Figure 1.

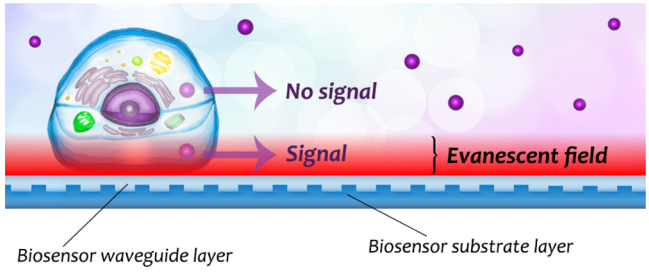

Figure 1. Schematic illustration of the concept of evanescent label-free biosensors in NP uptake detection. The evanescent field is a ∼150 nm thick layer above the biosensor surface. If there is a refractive index (RI) change in this zone (e.g., the NP reaches the evanescent field inside the cell), the biosensor detects this change and plots the shift in the wavelength ($\Delta\lambda$) real-time. If the NPs do not reach the evanescent field, there is no biosensor signal.

The sensor measures the alteration in the RI near the sensor surface. Optical label-free biosensors are excellent tools to examine the mode of action of small molecules and NPs as well.[1,32] For example, in our previous study,[32] we established that the positively charged AuNPs (stabilized by (11-mercaptoundecyl)-*N*,*N*,*N*-trimethylammonium bromide, TMA) can adsorb onto the biosensor surface and, together with the oppositely charged AuNPs (stabilized by 11-mercaptoundecanoic acid), can form clusters on the biosensor surface, monitored by optical waveguide lightmode spectroscopy. The main advantages of these label-free techniques are as follows: (i) they do not need any labels or additional chemicals that may disturb normal cell behavior or interactions with the cells, (ii) they can record real-time kinetic data with excellent resolution, and (iii) they are available in high-throughput formats, significantly decreasing the analysis time of complicated systems. Therefore, they were suggested as perfect candidates for investigating the NP−cell interaction and the kinetics and dynamics of the intracellular penetration of functionalized NPs.[1]

The main objective of this work is to examine the real-time kinetics of the cellular uptake of positively charged AuNPs by HeLa cells by using a label-free, high-throughput optical biosensor. In most of the studies on the NP−cell interaction, citrate-capped AuNPs were used;[13] these particles are negatively charged and the membrane of the cells is also negatively charged because of negatively charged groups in the lipid membrane. Therefore, we hypothesize that the cellular uptake of positively charged NPs would be more efficient, and thus, the toxicity would be optimal in the case of using positively charged NPs. We proved independently the cellular uptake by using TEM. In the kinetic experiments, NPs with different sizes were added to the adhered cells in different concentrations and the kinetics of the penetration into the cells as well as the adsorption of the AuNPs onto the biosensor surface were monitored. On the basis of control experiments using citrate-capped AuNPs of different sizes, we show that the efficiency of the cellular uptake of positively charged NPs by HeLa cells is not only strongly size-dependent but 1−2 orders of magnitude greater compared to the most widely used citrate-capped particles.

MATERIALS AND METHODS

Cell Culture and Cell Adhesion Assay Buffer. HeLa cells (ECACC 93021013 human, cervix, epitheloid, carcinoma) were cultured in tissue culture Petri dishes (Greiner Bio-One International GmbH, Kremsmünster, Austria) placed in a humidified incubator (37 °C, 5% CO_2). The cells were maintained in Dulbecco's modified Eagle's medium, completed with 4 mM L-glutamine, 10% fetal bovine serum (FBS, Biowest SAS, France), 100 U/mL penicillin, 100 μg/mL streptomycin solution, and 0.25 μg/mL amphotericin B. On reaching 80% confluence, the cells were detached every 3 days using 0.02% (w/v) ethylenediaminetetraacetic acid (EDTA) solution and 0.05% (w/v) trypsin.[33,34] An assay buffer for cell adhesion was prepared by adding 20 mM 4-(2-hydroxyethyl)-1-piperazine ethanesulfonic acid (HEPES, Sigma-Aldrich) to Hank's balanced salt solution (HBSS, Sigma-Aldrich), pH 7.0, with 1 mM NaOH.[33,35]

Synthesis and Functionalization of Positively Charged AuNPs. AuNPs were synthesized using gold (III) chloride trihydrate (Sigma-Aldrich) and functionalized with TMA (Sigma-Aldrich) using a wet synthesis procedure published in the literature.[36−42] Briefly, TMA was dissolved in dichloromethane, and, in a separate vial, presynthesized AuNPs were homogeneously dispersed in toluene. The thus-prepared solutions were mixed, and an excess amount of TMA was added to the AuNPs. Upon mixing, capping molecules on the surface of the AuNPs were exchanged to TMA. The resulting TMA-capped AuNPs were purified with methanol, dichloromethane, and toluene, using a rotary evaporator. The obtained particles had an average diameter size of 4.6 ± 0.4 nm based on TEM measurements. A stock solution of TMA-coated AuNPs (AuTMA) was prepared with a concentration of 15 mM (in terms of gold atoms). The number of TMA molecules per particle is 324, assuming that the adsorption area of thiol on gold is 0.214 nm^2 and the concentration of AuNPs was obtained from the absorbance at the maximum wavelength in the UV−vis spectrum (see Figure S1 in the Supporting Information). For

DOI: 10.1021/acsami.8b01546
ACS Appl. Mater. Interfaces 2018, 10, 26841−26850

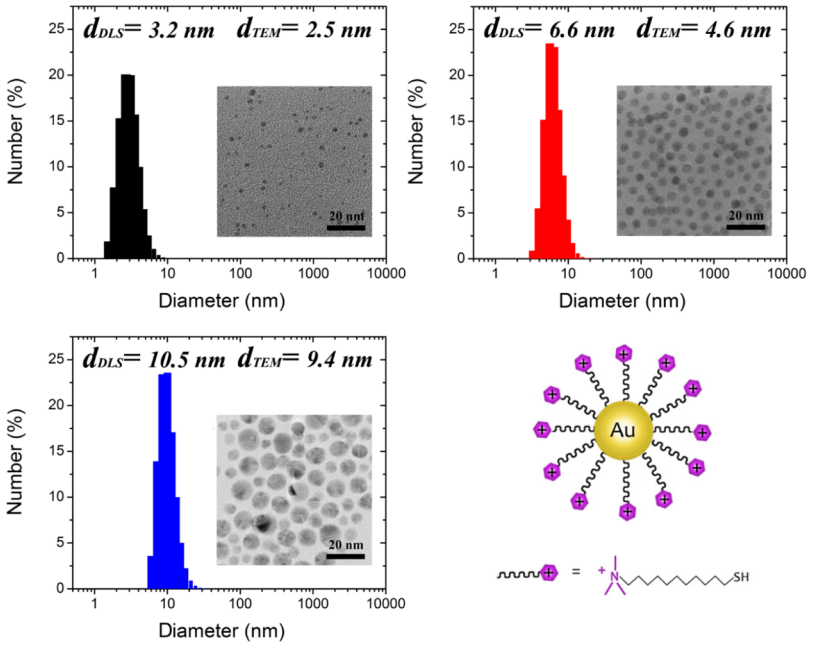

Figure 2. Size, size distribution by DLS measurements, and a schematic illustration of the AuNPs with three different sizes. The averaged sizes obtained from the DLS and TEM measurements are indicated.

further study, this stock solution was diluted with HBSS–HEPES to obtain NP solutions of 5.00, 0.50, and 0.05 mM (in terms of gold atoms). To investigate the size dependence of the cellular uptake, additionally, two different sizes of TMA-coated NPs were synthesized with the average sizes of 2.5 ± 0.3 and 9.4 ± 1.5 nm, respectively (Figure S1). TEM images and the size distributions of the AuNPs obtained are shown in Figure 2 with a schematic illustration of a single functionalized AuNP. We carried out dynamic light scattering (DLS) experiments on TMA-capped AuNPs as well; the polydispersity indices (PDIs) for different-sized particles of 2.5, 4.6, and 9.4 nm were 0.346, 0.379, and 0.248, respectively.

Synthesis of Citrate-Capped AuNPs. For control kinetic experiments, citrate-coated AuNPs of two different sizes were synthesized based on the procedures described in the studies of Shi et al.[43] and Piella et al.[44] For the synthesis of bigger citrate-capped AuNPs (d = 13.0 nm), we used gold (III) chloride trihydrate (Sigma-Aldrich) and trisodium citrate dihydrate (Sigma-Aldrich) as reducing and capping agents, respectively. Gold salt (25 mL) and 25 mL of trisodium citrate solutions of concentrations of 0.25 and 2.50 mM were prepared, respectively.[43] The gold salt solution was heated to 96 °C in an Erlenmeyer flask and was vigorously stirred at 500 rpm in a heating magnetic stirrer. After 10 min upon reaching the temperature of 96 °C, the preheated citrate solution was added to the hot gold solution. After 15 min, we switched off the heating and stirring. The synthesized citrate-capped AuNPs had an average size of 13.0 nm based on the DLS measurements with a PDI of 0.389 (Figures S2 and S3).

Smaller citrate-capped AuNPs (d = 5.5 nm) were synthesized by a modified citrate reduction method using tannic acid (Sigma-Aldrich).[44] A mixed solution containing 150 mL of trisodium citrate dehydrate (2.2 mM) and 0.1 mL of tannic acid (2.5 mM) was heated to 70 °C in an Erlenmeyer flask and was vigorously stirred at 500 rpm. After 10 min upon reaching the temperature of 70 °C, AuNPs were synthesized by injecting 1 mL of gold (III) chloride trihydrate solution (25 mM) into a mixed solution. After 10 min, we switched off the heating and stirring. The synthesized citrate-capped AuNPs had an average size of 5.5 nm based on the DLS measurements with a PDI of 0.507 (Figures S3 and S4).

Epic Benchtop Resonant Waveguide Grating Biosensor. The employed Epic Benchtop (BT) system (Corning Incorporated, Corning, NY, USA) is a resonant waveguide grating (RWG) imager biosensor, which accepts 96- or 384-well standard format biosensor microplates. A planar optical waveguide (made of niobium pentoxide) is incorporated at the bottom of each well.[33,35] Each waveguide contains a 2 × 2 mm optical grating to interrogate the TM_0 waveguide mode with near-infrared electromagnetic radiation. Therefore, individually addressable sensors are located in the microplate wells. The plate with all sensors is interrogated every 3 s by tuning the incoupled wavelength with a 0.25 pm precision in the range of 825–840 nm.[33,35] At the resonant wavelength (λ) of the optical structure, the waveguide mode is excited. RI variations above the sensor surface (in the ∼150 nm thick probing depth of the mode's evanescent wave) shift the resonant wavelength to λ'. A dynamic mass redistribution inside the adhered cells, cell spreading, bulk RI change, or molecular adsorption all can cause RI changes as the biomolecules have an RI larger than that of water.[33,35] The analyzed signals of the Epic BT system are the resonant wavelength shifts ($\Delta\lambda = \lambda' - \lambda$).[33,35]

AuNP Solutions in the Bare Biosensor Wells. After filling the plate wells with 30 μL HBSS–HEPES buffer, the baseline was taken by the biosensor. We pipetted 16 μL of the buffer to the wells and measured for 2 h to be comparable with the wells with cell addition (see below). After the 2 h period, solutions of AuNPs were added to the buffer (we pipetted 22 μL of the solutions of AuNPs into the wells, and we also added 22 μL of the buffer into the control wells). The AuNPs were measured for 2 h again. All measurements were done in triplicate. The schematic illustration of the method and measurements is shown in Figure 3.

AuNP Treatment of the Cells on the Biosensor Surface. After filling the plate wells with HBSS–HEPES, the baseline was taken by the biosensor. HeLa cells were trypsinized with a warm trypsin–EDTA solution. Trypsin was replaced before complete detachment of the cells, and its activity was inhibited by adding culture medium containing 10% FBS. Harvested cells were centrifuged for 6 min at 2000 rpm, and the cell pellet was suspended in the assay buffer. The cells were counted in a hemocytometer, and 20 000 cells were pipetted to the wells with 30 μL of the assay buffer inside. We added 16 μL from the cell suspension into the wells, and we also added 16 μL of the buffer into the control wells, which did not contain any cells. The cells were measured for 2 h to let them spread. After this period, solutions of AuNPs were added to the cells (we pipetted 22 μL of the solutions of AuNPs into the wells, and we also added 22 μL of the buffer into the control wells). The HeLa cells were measured for an additional 2 h. All measurements were done in triplicate. The

DOI: 10.1021/acsami.8b01546
ACS Appl. Mater. Interfaces 2018, 10, 26841–26850

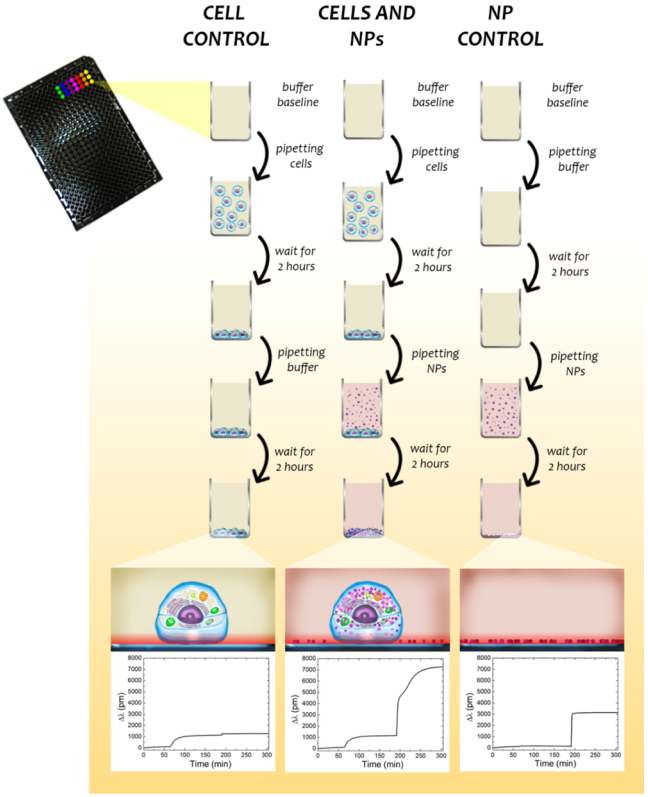

Figure 3. Schematic illustration of the method and the process of the biosensor measurements. All experiments (cell control, NP control, and the cells treated with different concentrations of AuNP solutions) were performed in triplicate simultaneously, allowed by the plate format (for all types of measurements, one representative experiment is shown). The typical kinetic curves recorded are also shown in the bottom of the image.

schematic illustration of the method and measurements is shown in Figure 3.

Optical Microscopy of the Cells. At the end of the Epic BT biosensor experiments, the microplate was put into a Zeiss Axiovert Observer microscope to image the cells.[33,35] The three-dimensional images of the adhered cells were also recorded by a digital holographic microscope.[34]

Fixation of the NP-Treated Cells. HeLa cells were grown in 25 cm^2 flasks until confluency. Then, the cell culture medium was replaced by different concentrations of AuNPs suspended in the HBSS–HEPES buffer. The cells were incubated with AuNPs for 2 h in a CO_2 incubator, trypsinized and washed twice with HBSS–HEPES, and then were fixed for 24 h at 4 °C (3.2% paraformaldehyde, 0.2% glutaraldehyde, 40 mM $CaCl_2$, 1.0% sucrose in 0.1 M cacodylate buffer, pH 7.2). After 1 h treatment, the pellets were gently dislocated from the tube wall for perfect penetration.

Sample Preparation for TEM Investigation. TEM investigation was performed for TMA-coated AuNPs, and the samples were rinsed for 24 h in 0.1 M cacodylate buffer containing 1% sucrose, 40 mM $CaCl_2$, washed in 0.1 M cacodylate buffer (5 min twice), and then treated with 1% osmium tetroxide (1 h at room temperature). After washing in cacodylate buffer and distilled water, the pellets were reacted with 1% aqueous uranyl acetate (30 min). Dehydration was carried out with ascending grades of alcohol (25, 50, 75, and 96% ethyl alcohol for 5 min each) and absolute ethanol (10 min three times). Samples were impregnated with acetonitrile solution (10 min twice), with an equal ratio mixture of Spurr-acetonitrile (60 min) and finally with pure Spurr low-viscosity epoxy resin medium (Sigma-Aldrich, 60 min twice). Polymerization was carried out at 80 °C for 48 h. Ultrathin sections were cut with a diamond knife (Diatome) in a Reichert OM UIII ultramicrotome. Sections were stained with 2.5% aqueous uranyl acetate (10 min) and Reynolds's lead citrate (3 min) and then were examined by a JEOL JEM 1011 transmission electron microscope equipped with a Morada 11 megapixel camera and iTEM software (Olympus).

RESULTS AND DISCUSSION

NP Adsorption onto the Bare Biosensor Surfaces. First, we investigated the interaction of the solutions of 4.6 nm AuNPs with the bare Epic sensor surfaces (without adhered cancer cells). The results of the Epic BT measurements are shown in Figure 4A. The buffer control did not show any

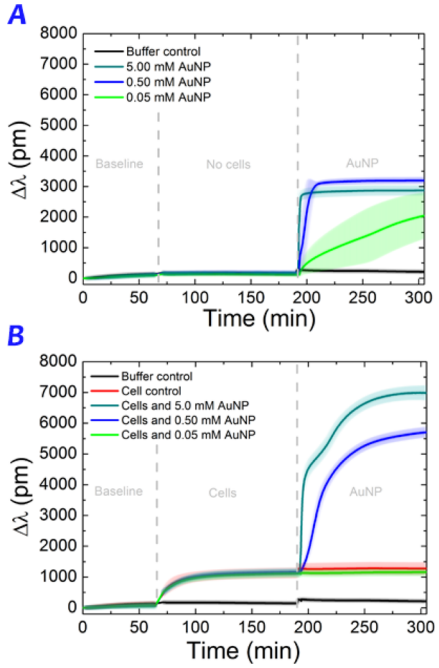

Figure 4. Averaged kinetic curves recorded by the Epic BT high-throughput label-free optical biosensor. (A) Adsorption of the 4.6 nm TMA-functionalized AuNPs with different concentrations onto the biosensor surface. (B) Kinetics of interactions of the 4.6 nm TMA-functionalized AuNPs with adhered cancer cells.

wavelength shift; the signal stayed at around 0 pm (black kinetic curve). The 0.05 mM AuNP solution showed a long-drawn signal, which reached a wavelength shift of around 2000 pm (green kinetic curve). The other two higher concentrations of AuNP solutions (0.5 and 5 mM, blue and cyan kinetic curves) gave larger signals with fast saturation at around 3000 pm (Figure 4A). It is seen that the two larger concentrations saturate the surface; clearly, no more space is available for further NP adsorption. We attribute the slightly larger saturation value in the case of the 0.5 mM solution to the slower adsorption process, which results in a larger packaging density of the NPs.

An important question can be raised whether the AuNPs adsorbed onto the biosensor surface or they just floated in the evanescent field without adsorbing on the surface. One can conclude that even the thickest solution would only give an RI increment compared to water of 10^{-3}, equivalent to a 127 pm wavelength shift.[45] Therefore, the 3000 pm wavelength shift observed is due to the adsorption of NPs onto the bare biosensor surface. The NP control curves show quick adsorption onto the surface, especially in the case of the 5.00 and 0.50 mM NP solutions (Figure 4A, dark cyan and blue

DOI: 10.1021/acsami.8b01546
ACS Appl. Mater. Interfaces 2018, 10, 26841–26850

Table 1. Concentration, Wavelength Shift ($\Delta\lambda$), Calculated Adsorbed Mass (ΔM), and Number of AuNPs Are Summarized at the End of the Adsorption Processes on the Bare Biosensor Surface

concentration						
(mM)	(mg/mL)	$\Delta\lambda$ (pm)	ΔM (ng/cm^2)	number of NPs/mm^2	number of NPs/100 × 100 nm^2	number of NPs/mL
0.05	0.0098	2047.25 ± 683.43	323.47 ± 107.98	3.3×10^9	33	1.00×10^{13}
0.50	0.098	3197.98 ± 43.6	505.28 ± 6.87	5.16×10^9	52	1.00×10^{14}
5.00	0.98	2874.69 ± 97.91	454.24 ± 15.56	4.64×10^9	46	1.00×10^{15}

kinetic curves). From the saturation of the NP control kinetic curves, we can declare that the AuNPs form an adsorbed monolayer on the bare biosensor surface (Figure 4A, dark cyan and blue kinetic curves).

The adsorbed mass can be calculated from the Epic BT data. The wavelength shift [$\Delta\lambda$ (pm)] can be easily converted to a surface-adsorbed mass (ng/cm^2) by using the calibration equation of Orgovan et al.[45] Note that the equation is valid for a polyelectrolyte solution with an RI increment of dn/dc = 0.1955 cm^3/g. The dn/dc value of the AuNP solution is 0.383 cm^3/g as determined earlier by measuring the RI of the AuNP solutions using a tabletop refractometer.[32] On the basis of the previously developed methodology,[45] this value leads to the following calibration equation:

$$\Delta M = 0.158 \text{ ng/(pm cm}^2) \times \Delta\lambda \quad (1)$$

where ΔM is the surface-adsorbed NP mass (ng/cm^2) and $\Delta\lambda$ is the measured wavelength shift (pm).

The number of NPs can be determined by using the parameters of a single NP, namely, the diameter, the density of gold (19 320 kg/m^3), and using the perfect-sphere approximation. The mass of a single AuNP is 9.8×10^{-10} ng. (Note that on the basis of a typical surface coverage value of 100 ng/cm^2, the mass of the coating is more than an order of magnitude less and was neglected.)

The adsorbed amount (ΔM) and surface densities of the adsorbed AuNPs on the biosensor surface are calculated and shown in Table 1.

Interaction of NPs with the Cell-Covered Biosensor Surfaces. Next, the effect of the solutions of the AuNPs was investigated in the biosensor wells coated with living cells. Microscopy images confirmed that the HeLa cells covered roughly 50% of the sensor surface with an averaged single cell area of around 500 μm^2 (Figure S5A,B).

Figure 5 summarizes all the possible interactions of the AuNPs and the cells in this case. (A) AuNPs can reach the bare sensor surface by diffusion without even touching the surface of the cells. (B) NPs can adsorb on the cell surface, desorb, and diffuse to the bare sensor surface. (C) NPs irreversibly adsorb on the surface of the cells. (D) NPs adsorb on the surface of the cell, penetrate into the cell, and reach the evanescent field. (E) NPs penetrate into the cell but do not reach the evanescent field.

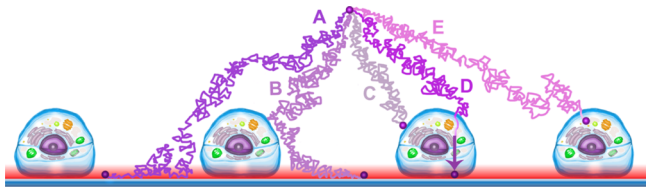

Figure 5. Possible paths of a single AuNP (purple sphere). The AuNP moves in the liquid by Brownian motion. (A) AuNPs adsorb onto the sensor surface without reaching the cells. (B) AuNPs just reach the cell surface but cannot penetrate; they move on and adsorb onto the biosensor surface. (C) AuNPs reach the surface of the cell and stay there. (D) AuNPs reach the surface of the cell, penetrate, and reach the evanescent field inside the cell. (E) AuNPs reach the surface of the cell and penetrate but do not reach the evanescent field inside the cell.

In case A, the AuNPs do not interact with the cells, and the corresponding biosensor signals shown in Figure 4A should be simply divided by 2 because of the ∼50% available bare sensor surface. In contrast, the measured signals are strongly deviating from this noninteracting behavior (Figure 4B). The investigation of the slopes of the kinetic curves right after the AuNP addition for the bare and cell-covered surfaces is also revealing (summarized in Table 2).

Table 2. Initial Slopes of the Kinetic Curves Right after AuNP Addition in the Case of a Bare Surface and an ∼50% Cell-Covered Surface

concentration (mM)	initial slope on the bare surface (pm/min)	initial slope on the ∼50% cell-covered surface (pm/min)
0.05	56 ± 2	0
0.50	529 ± 43	66 ± 5
5.00	>4000[a]	781 ± 8

[a]There were not enough points to evaluate the exact value of the initial slope.

The following equation is valid for the initial slope ($d\lambda/dt$):

$$d\lambda/dt \approx kcA \quad (2)$$

where k is the adsorption rate constant, c is the concentration of NPs, and A is the available sensor area. Again, in a noninteracting case, the slopes recorded in the bare surface should be divided by 2 to get the slopes in the experiments with the adhered cells. In contrast, large deviations are seen from this noninteracting behavior in Table 2.

Surprisingly, using the lowest NP concentration, no signal is observed. This suggests that the AuNPs do not at all reach the evanescent field. Importantly, they do not even adsorb at the bare areas of the sensor surface. The data clearly suggest that at least they are adsorbing on the surfaces of the cells (path C or E). Therefore, the interaction between the surface of the cells and the NPs is clearly proven by the recorded data. This hypothesis is further supported by investigating the diffusion times. From a simple diffusion distance calculation (supposing a 10^{-7} cm^2/s diffusion coefficient), AuNPs move 10 μm during 10 s by diffusion. This is a very small value compared to the time when they saturate the surface in the case of the 0.05 mM solution. Indeed, AuNPs can realistically reach the surfaces of the cells before adsorbing onto the bare areas. This phenomenon obviously dominates for the 0.50 mM concentration solution as well, and just as in the case of the highest concentration, the diffusion time is comparable with the saturation time at the bare sensor. Note that here a shoulder

DOI: 10.1021/acsami.8b01546
ACS Appl. Mater. Interfaces 2018, 10, 26841−26850

also appears on the kinetic curve (Figure 4B). At the highest concentration, some of the AuNPs can adsorb onto the bare sensor areas without interacting with the cells. However, for the two highest concentrations, the observed signals are largely increased compared to the signals measured on the bare surfaces, proving that in some way the cells help the accumulation of the AuNPs inside the evanescent field (path D). Therefore, we can safely conclude that at the two highest concentrations, the AuNPs not only reach the surface of the cells but also penetrate into the cells and effectively reach the evanescent filed. The number of NPs penetrated into the evanescent field can be estimated by the measured wavelength shifts and using eq 1. Supposing an averaged cell area of 500 μm^2, roughly 2.2 and 3.3 pg mass increase per cell was recorded in the case of the 0.5 nM and the 5 mM solutions, respectively. Moreover, on the basis of the 0.25 pm sensitivity of the biosensor,[45] the values in Table 1 and the averaged single cell area of 500 μm^2 lead to the minimum detectable number of NPs per cell to be around 4. Note that on the basis of the sensitivity data presented in ref 46, the state-of-the-art ICP−MS technique is around 2 orders of magnitude more sensitive.

The penetration of the AuNPs into the HeLa cells is further supported by the shape of the kinetic curves, showing a sigmoidal character, a typical feature of active, living processes. Therefore, we further suppose that the AuNPs are internalized into the cells by an active process. For a more detailed structural analysis about the fate of the NPs, we performed TEM experiments on the NP-exposed and fixed cells. To highlight the kinetics of cellular uptake of positively charged AuNPs by HeLa cells, we carried out similar kinetic experiments with two different-sized citrate-capped negatively charged AuNPs (d = 5.5 ± 0.3 nm and d = 13.0 ± 0.7 nm, Figure S6). In this case, we also started our investigation with the interaction of the AuNPs with the bare Epic sensor surfaces. We recorded a wavelength shift of ∼220 pm at the highest concentration (5.00 mM) of the citrate-capped AuNPs. This shift is less than in the case of the TMA-coated AuNPs as the surface of the biosensor is slightly negatively charged. The other two lower concentrations of AuNP solutions containing smaller and bigger citrate-capped NPs provided lower signals. Most importantly, with cells present on the surface, the maximum shift observed was in the case of using NPs of 13.0 nm; even this is 26 times less compared to the case of the TMA-coated 4.6 nm sized AuNPs (Figure S6C,D). It is important to note that the citrate-capped NPs with the size of 5.5 nm generated a wavelength shift of 117 times less compared to the case of the TMA-coated AuNPs (Figure S6C).

Role of NP Size: Verification of Optimal Size for Cellular Uptake. During the biosensor experiments, we employed positively charged AuNPs with a diameter of ∼5 nm because of their optimal size and charge for penetration into the Rat2 fibroblast cells, according to previous findings.[12] To verify this observation in the case of HeLa cells, we performed the above-mentioned biosensor experiment with smaller (2.5 nm) and larger (9.4 nm) NPs with a concentration of 0.5 mM. The results showed that the NPs with a 9.4 nm diameter adsorbed onto the biosensor surface by the highest number (Figure 6A); however, the ∼5 nm positively charged NPs penetrated into the cells and reached the evanescent field most intensively (Figure 6B), well confirming the results of Pillai et al.[12] The results obtained with the living cells are further

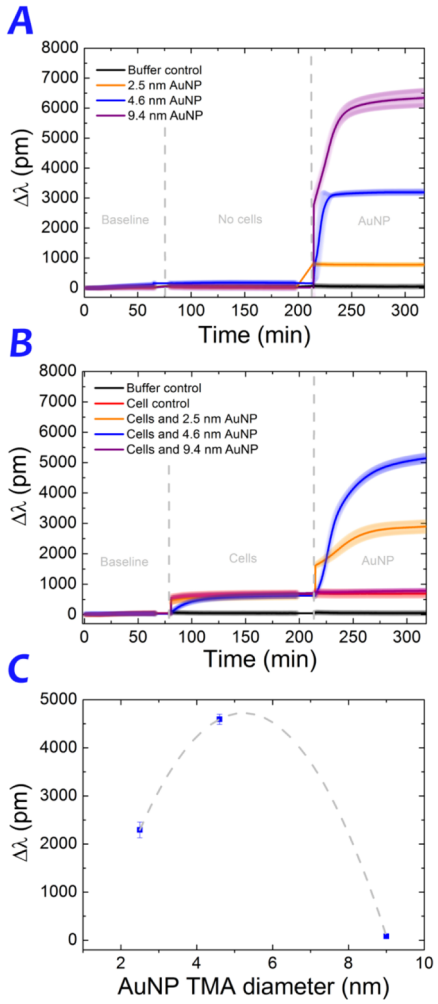

Figure 6. Averaged kinetic curves of the TMA-functionalized AuNPs with different diameter sizes with a 0.5 mM concentration. (A) Adsorption of the TMA-functionalized AuNPs onto the biosensor surface. (B) Kinetics of the interactions of the TMA-functionalized AuNPs with the adhered cancer cells. (C) Biosensor signal increases after NP addition to the cells adhered on the sensor surfaces. The diameter of 4.6 nm resulted in the largest effect, confirming an optimal size for cellular uptake. The dotted line is only to guide the eye.

emphasized in Figure 6C, where the signal changes after the NP treatment of the adhered living cells are plotted. Even if we investigated only three NP sizes, the tendency is clearly seen; the addition of both smaller (2.5 nm) and larger (9.4 nm) TMA-coated particles resulted in a smaller signal increase than that observed for the 4.6 nm sized NPs.

Verification of NP Cellular Uptake by TEM. We observed NPs on the cell surface and in relatively deep, tubular-shaped plasma membrane invaginations. The membrane-associated AuNPs formed aggregates (Figure 7B,C). The internalized particles were detectable only in membrane-bordered compartments in the cytoplasm (Figure 7A). This observation excludes the possibility that the AuNPs get into the cells directly through the lipid bilayer of the plasma membrane in a nonregulated manner or by membrane damage.

The mentioned membrane-bordered compartments correspond to the members of the endosomal−lysosomal system (ELS) of the cells.[47] The ELS is specialized in uptake, sorting, recycling, and degrading of incoming substances (nutrients,

DOI: 10.1021/acsami.8b01546
ACS Appl. Mater. Interfaces 2018, 10, 26841−26850

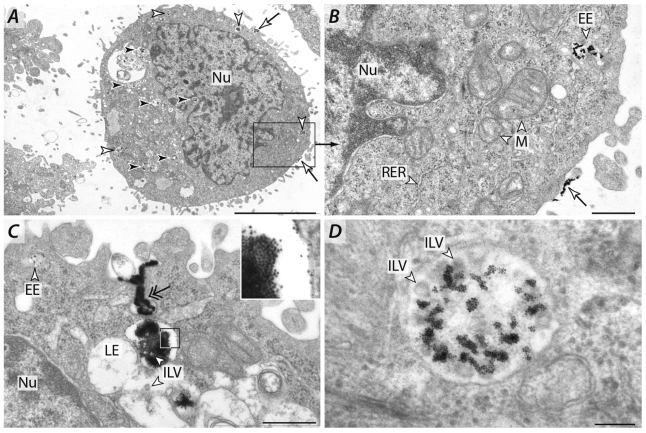

Figure 7. Cellular localization of TMA-functionalized AuNPs (d = 4.6 nm). (A) Overview of a cell after internalization of AuNPs. AuNPs are detectable as a black precipitate on the cell surface (arrows with white arrowhead), in the elements of the EE and late endosomal (LE) system (white and black arrowheads, respectively). (B) Magnified area of panel A. The positively charged NPs form aggregates on the plasma membrane (white arrow) and in irregular-shaped EE directly beneath the cell surface. (C) Uptake of NPs takes place by forming a deep plasma membrane invagination which has a tubular stalk and a globular ending (arrow with double heads). Small aggregates are seen in a vesicle that belongs to the EE system. AuNPs accumulate in the extended LE compartment which contains the ILVs. Inset: note the discrete AuNPs in the lumen of the LE element. (D). MVB with ILVs and accumulated gold particles among them (M—mitochondrion, Nu—nucleus, RER—rough endoplasmic reticulum; scale bars: (A) 5 μm, (B,C) 500 nm, and (D) 100 nm).

extracellular matrix, etc.).[48] Accordingly, at first the internalized AuNPs reached the early endosomal (EE) subcompartment, which is identifiable on the basis of its small diameter (Figure 7C) or irregular shape and its localization in the close vicinity of the plasma membrane (Figure 7B). Processing of the internalized material takes place in the round-shaped late endosomal components. These organelles locate in the perikaryonal cytoplasm and may also contain cytoplasmic elements directed to degradation. A characteristic member of this subcompartment of the ELS is the multivesicular body (MVB), which has small intraluminal vesicles (ILVs) enclosing the material originated from the cytoplasm. TMA-coated AuNPs accumulated in the MVBs among these ILVs (Figure 7D).

There exist many routes of endocytic uptake into cells. The internalization of AuNPs is presumably a fast event because it is very rarely observed at the ultrastructural level. The exact mechanism is questionable, but the morphology of the plasma membrane invagination with a long tubular stalk and flared, vesicular ending (Figure 7C) raises a possibility of both the caveolae/caveolin1-dependent and the CLIC (clathrin-independent carriers)/GEEC (glycosylphosphotidylinositol- anchored protein (GPI-AP) enriched early endosomal compartments)-like endocytosis.[49−51] Both pathways are evolved for the uptake of glycosylphosphatidylinositol (GPI)-anchored proteins (APs), which frequently form nanometer-scale clusters in the plasma membrane. Similar to the TMA-coated NPs on the HeLa cell surface, GPI-AP clusters with their membrane microdomains move together even during internalization. Furthermore, the CLIC/GEEC pathway is thought to contribute to an important fraction of the overall fluid-phase uptake of the cell.[51]

Using an adequate concentration (0.50 and 0.05 mM) of AuNPs, the internalized AuNPs were never seen separately in the cytosol; they concentrated in membrane-bound vacuolar elements of the ELS (Figure 7). However, a treatment with a high concentration (5.00 mM) of NPs impaired the cells (Figure 8A) and destroyed the lysosomal membrane, causing

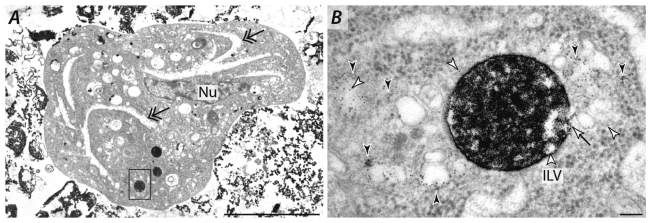

Figure 8. Severely damaged cell after treatment with a high concentration of AuNPs (5.00 mM, d = 4.6 nm). (A) Overview of an intact but damaged cell with strange, swollen slitlike spaces (arrow with double heads). Cell debris intensely decorated by AuNPs surrounding it. (B) Magnified area of panel A. MVB with ILVs: the space between ILVs is filled with AuNPs. The outer membrane of the MVB is leaky (arrow with white head), and several AuNPs are visible in the cytoplasm (black arrowheads). Some discrete AuNPs are also detectable in the cytoplasm (white arrowheads; scale bars: (A) 5 μm, (B) 100 nm).

AuNPs' and lysosomal enzyme leakage (Figure 8B). Lysosomal membrane disruption and leakage of the lysosomal content into the cytosol lead to "lysosomal cell death".[52]

We did not observe any single NP adsorption to the cell surface. The AuNPs accumulate in the endosome from different parts of the cells, but on the membrane we should have seen single particles, if they aggregate in the solution itself.

Certainly, it is not impossible that the AuNPs start to aggregate in the liquid during storage, but generally, there is no aggregation in the solution proved by the UV−vis spectra (Figure S1) and DLS experiments (Figure 2). Furthermore, we diluted the stock solutions, so if there were aggregated particles, we should have seen them in the diluted liquid as well. The cells were treated by AuNPs diluted in HBSS−HEPES buffer, which contains K^+, Na^+, Mg^{2+}, Ca^{2+}, Cl^-, $HPO_4^{2-}/H_2PO_4^-$ ions (all together 155 mM, mainly NaCl) and 2 mM glucose. The control experiments proved that these components do not induce aggregation of AuNPs, so there are free and unaggregated NPs in the solution (Figure S7). The fixation liquid contains glutaraldehyde, formaldehyde, sugar, Ca^{2+}, and Na-cacodylate. From the experience of decades and our control experiments, we can declare that these chemicals do not cause aggregation of the NPs or artifact either (Figure S7).

Discrete AuNPs were rarely detected only in the LE elements (MVBs) and the cytoplasm after lysosomal damage. One possibility that the TMA-coated AuNPs dissociate from hypothesized GPI-APs (receptors) may have contributed to their aggregated internalization. The maturation of the EEs is a gradual process that creates a unique acidic environment in the LEs (MVBs) and lysosomes.[53] The binding of the ligand to the receptor is dependent on the pH[54] and the luminal pH reduction causes ligand dissociation from the receptor.[48] Another possibility is that lysosomal enzymes digest the hypothesized GPI-APs or alter the coat of the AuNPs. Moreover, the appearance of discrete NPs is not a general

DOI: 10.1021/acsami.8b01546
ACS Appl. Mater. Interfaces 2018, 10, 26841−26850

phenomenon; therefore, clarifying the exact mechanism requires further studies.

Another important question is whether the positive charge has some kind of a role in the penetration of the NPs. It has been shown that the positively charged AuNPs adsorb to the membrane more easily and internalize more effectively than the negatively charged AuNPs.[12] The surface of the mammalian cells is full of sialic acid, so it is negatively charged. Thus, the smallest negatively charged molecules do not get through either. (The apolar ones fade into the membrane but do not come into the cytoplasmic side.) The AuNPs with a diameter of 4.6 nm are too large to get through the membrane even though they are positively charged. The other mechanism is the penetration via receptors, which can be specific to a molecule (e.g., insulin receptor), but the larger molecules or particles get into the cells by phagocytosis or by the receptors which recognize some kind of molecular markers (for instance, sugars from side chains of proteins). In this case, the medium size is favorable because it can tie a lot of receptors simultaneously and contracts the receptors on certain parts of the membrane, and thus an active process can start, which ends in the internal attachment of the membrane. Therefore, still unidentified receptors may participate in AuNPs' intake as well.

CONCLUSIONS

In this proof-of-principle study, we monitored the penetration of 4.6 nm sized TMA-functionalized (positively charged) AuNPs into adhered HeLa cells by using a high-throughput evanescent-field-based optical biosensor in a real-time and completely label-free way. Because of the employed plate-based format, numerous measurements can be carried out simultaneously; thus, the experiments were relatively easy and fast. We showed that resonant waveguide-based techniques are well-suited for studying the cellular uptake of AuNPs. Importantly, because of the in situ measurement platform, not only can the last stage of the experiments and interactions be observed, but the kinetics of the interactions can also be analyzed in a cost-effective manner with excellent time resolution. The shape of the recorded kinetic curves suggested that the AuNPs are internalized into the cells by an active process. In the case of penetration of NPs into the cells, and especially in further NP-based therapies, the dynamics of uptake is important and may have additional information in store. The present configuration can also find applications in optimizing the functional coatings of NPs in a straightforward manner. We carried out control kinetic experiments using citrate-capped (negatively charged) AuNPs and TMA-coated NPs with smaller (2.5 nm) and larger (9.4 nm) sizes. These experiments proved that their cellular uptake is less effective than that of the 4.6 nm sized TMA-coated NPs. This finding supports our hypothesis that the cell membrane and NPs' interaction plays a crucial role in the penetration of the charged NPs as the membrane composition of the cells is negatively charged; thus, an attractive electrostatic interaction can help NPs to be internalized into the cells.

The conclusions based on the biosensor data were further confirmed using TEM. We observed NPs on the cell surface and in relatively deep, tubular-shaped plasma membrane invaginations by using TEM. The internalized particles were detectable only in membrane-bordered compartments in the cytoplasm. This observation with the electron microscopy excludes the possibility that the AuNPs get into the cells directly through the lipid bilayer of the plasma membrane in a nonregulated manner or by membrane damage. The mentioned membrane-bordered compartments correspond to the members of the ELS of the cells. TMA-coated AuNPs were accumulated in MVBs among small ILVs. Using an adequate concentration (0.50 and 0.05 mM) of AuNPs, the internalized AuNPs were never seen separately in the cytosol; they concentrated in membrane-bound vacuolar elements of the ELS. The exact mechanism is questionable, but the morphology of the plasma membrane invagination with a long tubular stalk and a flared, vesicular ending raises the possibility of both the caveolae/caveolin1-dependent and the CLIC/GEEC-like endocytosis.[49−51] The appearance of discrete NPs is not a general phenomenon; therefore, clarifying the exact mechanism requires further studies.

Besides the advantages of the introduced approach, such as real-time, label-free, and fast detection, it has also some limitations. In the case of the 0.05 mM AuNP solution, there is no detectable signal in the evanescent field when the NPs interact with the adhered cells. However, TEM revealed that only a small number of NPs penetrate into the cells. Note that if the AuNPs move above the evanescent field, we cannot obtain any signal by the present biosensor. Therefore, an important way would be to develop biosensors with greater penetration depth of the evanescent field, to possibly detect NP admission for the lower concentrations of NPs as well. The adaptation of deep-probing sensors[55−59] into high-throughput formats would find interesting applications in the present field.

ASSOCIATED CONTENT

Supporting Information

The Supporting Information is available free of charge on the ACS Publications website at DOI: 10.1021/acsami.8b01546.

UV−vis spectra of positively charged and citrate-capped (negatively charged) AuNPs; size distributions of the citrate-capped AuNPs obtained by DLS measurements; microscopic images of the HeLa cells; kinetic curves recorded by an optical biosensor using citrate-capped AuNPs; and stability of positively charged NPs in buffers and the fixation liquid (PDF)

AUTHOR INFORMATION

Corresponding Author

*E-mail: horvath.robert@energia.mta.hu.

ORCID

Istvan Lagzi: 0000-0002-2303-5965
Hideyuki Nakanishi: 0000-0001-8065-6373
Dániel Zámbó: 0000-0001-7671-039X
András Deák: 0000-0002-2526-1245
Robert Horvath: 0000-0001-8617-2302

Notes

The authors declare no competing financial interest.

ACKNOWLEDGMENTS

This work was supported by the Momentum Program ("Lendület") of the Hungarian Academy of Sciences and by the ERC_HU and KH_17 programs of NKFIH. The project was subsidized by the European Union and cofinanced by the European Social Fund. R.H., I.L., and L.C. were supported by the MedinProt Synergy project. H.N. acknowledges the funding support from JSPS KAKENHI grant numbers

DOI: 10.1021/acsami.8b01546
ACS Appl. Mater. Interfaces 2018, 10, 26841−26850

JP18H01828 and JP16K13627, the Iwatani Naoji Foundation, the Ogasawara Foundation for the Promotion of Science & Engineering, and the Project for Enhancing Research and Education in Polymer and Fiber Science at KIT.

REFERENCES

(1) Peter, B.; Bosze, S.; Horvath, R. Biophysical characteristics of proteins and living cells exposed to the green tea polyphenol epigallocatechin-3-gallate (EGCg): review of recent advances from molecular mechanisms to nanomedicine and clinical trials. *Eur. Biophys. J.* **2017**, *46*, 1−24.

(2) Song, Q.; Li, D.; Zhou, Y.; Yang, J.; Yang, W.; Zhou, G.; Wen, J. Enhanced uptake and transport of (+)-catechin and (-)-epigallocatechin gallate in niosomal formulation by human intestinal Caco-2 cells. *Int. J. Nanomed.* **2014**, *9*, 2157−2165.

(3) Lee, H.-Y.; Shin, S. H. R.; Abezgauz, L. L.; Lewis, S. A.; Chirsan, A. M.; Danino, D. D.; Bishop, K. J. M.; Bishop, K. J. M. Integration of Gold Nanoparticles into Bilayer Structures via Adaptive Surface Chemistry. *J. Am. Chem. Soc.* **2013**, *135*, 5950−5953.

(4) Wu, G.; Mikhailovsky, A.; Khant, H. A.; Fu, C.; Chiu, W.; Zasadzinski, J. A. Remotely Triggered Liposome Release by Near-Infrared Light Absorption via Hollow Gold Nanoshells. *J. Am. Chem. Soc.* **2008**, *130*, 8175−8177.

(5) Volodkin, D. V.; Skirtach, A. G.; Möhwald, H. Near-IR Remote Release from Assemblies of Liposomes and nanoparticles. *Angew. Chem., Int. Ed.* **2009**, *48*, 1807−1809.

(6) Kennedy, L. C.; Bickford, L. R.; Lewinski, N. A.; Coughlin, A. J.; Hu, Y.; Day, E. S.; West, J. L.; Drezek, R. A. A New Era for Cancer Treatment: Gold-Nanoparticle-Mediated Thermal Therapies. *Small* **2011**, *7*, 169−183.

(7) Gopalakrishnan, G.; Danelon, C.; Izewska, P.; Prummer, M.; Bolinger, P.-Y.; Geissbühler, I.; Demurtas, D.; Dubochet, J.; Vogel, H. Multifunctional Lipid/Quantum Dot Hybrid Nanocontainers for Controlled Targeting of Live Cells. *Angew. Chem., Int. Ed.* **2006**, *45*, 5478−5483.

(8) Chen, Y.; Bose, A.; Bothun, G. D. Controlled Release from Bilayer-Decorated Magnetoliposomes via Electromagnetic Heating. *ACS Nano* **2010**, *4*, 3215−3221.

(9) Amstad, E.; Kohlbrecher, J.; Müller, E.; Schweizer, T.; Textor, M.; Reimhult, E. Triggered Release from Liposomes through Magnetic Actuation of Iron Oxide Nanoparticle Containing Membranes. *Nano Lett.* **2011**, *11*, 1664−1670.

(10) Wang, S.; Su, R.; Nie, S.; Sun, M.; Zhang, J.; Wu, D.; Moustaid-Moussa, N. Application of Nanotechnology in Improving Bioavailability and Bioactivity of Diet-Derived Phytochemicals. *J. Nutr. Biochem.* **2014**, *25*, 363−376.

(11) Lu, Y.-C.; Luo, P.-C.; Huang, C.-W.; Leu, Y.-L.; Wang, T.-H.; Wei, K.-C.; Wang, H.-E.; Ma, Y.-H. Augmented Cellular Uptake of Nanoparticles Using Tea Catechins: Effect of Surface Modification on Nanoparticle-Cell Interaction. *Nanoscale* **2014**, *6*, 10297−10306.

(12) Pillai, P. P.; Huda, S.; Kowalczyk, B.; Grzybowski, B. A. Controlled pH Stability and Adjustable Cellular Uptake of Mixed-Charge Nanoparticles. *J. Am. Chem. Soc.* **2013**, *135*, 6392−6395.

(13) Alkilany, A. M.; Murphy, C. J. Toxicity and Cellular Uptake of Gold Nanoparticles: What We Have Learned so Far? *J. Nanopart. Res.* **2010**, *12*, 2313−2333.

(14) Chithrani, B. D.; Ghazani, A. A.; Chan, W. C. W. Determining the Size and Shape Dependence of Gold Nanoparticle Uptake into Mammalian Cells. *Nano Lett.* **2006**, *6*, 662−668.

(15) Hauck, T. S.; Ghazani, A. A.; Chan, W. C. W. Assessing the Effect of Surface Chemistry on Gold Nanorod Uptake, Toxicity, and Gene Expression in Mammalian Cells. *Small* **2008**, *4*, 153−159.

(16) Cho, E. C.; Liu, Y.; Xia, Y. A Simple Spectroscopic Method for Differentiating Cellular Uptakes of Gold Nanospheres and Nanorods from Their Mixtures. *Angew. Chem., Int. Ed.* **2010**, *49*, 1976−1980.

(17) Cho, E. C.; Xie, J.; Wurm, P. A.; Xia, Y. Understanding the Role of Surface Charges in Cellular Adsorption versus Internalization by Selectively Removing Gold Nanoparticles on the Cell Surface with a I2/KI Etchant. *Nano Lett.* **2009**, *9*, 1080−1084.

(18) Au, L.; Zhang, Q.; Cobley, C. M.; Gidding, M.; Schwartz, A. G.; Chen, J.; Xia, Y. Quantifying the Cellular Uptake of Antibody-Conjugated Au Nanocages by Two-Photon Microscopy and Inductively Coupled Plasma Mass Spectrometry. *ACS Nano* **2010**, *4*, 35−42.

(19) Alkilany, A. M.; Nagaria, P. K.; Hexel, C. R.; Shaw, T. J.; Murphy, C. J.; Wyatt, M. D. Cellular Uptake and Cytotoxicity of Gold Nanorods: Molecular Origin of Cytotoxicity and Surface Effects. *Small* **2009**, *5*, 701−708.

(20) Patil, S.; Sandberg, A.; Heckert, E.; Self, W.; Seal, S. Protein adsorption and cellular uptake of cerium oxide nanoparticles as a function of zeta potential. *Biomaterials* **2007**, *28*, 4600−4607.

(21) Hsiao, I.-L.; Bierkandt, F. S.; Reichardt, P.; Luch, A.; Huang, Y.-J.; Jakubowski, N.; Tentschert, J.; Haase, A. Quantification and Visualization of Cellular Uptake of TiO2 and Ag Nanoparticles: Comparison of Different ICP-MS Techniques. *J. Nanobiotechnol.* **2016**, *14*, 1−13.

(22) Mueller, L.; Traub, H.; Jakubowski, N.; Drescher, D.; Baranov, V. I.; Kneipp, J. Trends in Single-Cell Analysis by Use of ICP-MS. *Anal. Bioanal. Chem.* **2014**, *406*, 6963−6977.

(23) Adjei, I. M.; Sharma, B.; Labhasetwar, V. Nanoparticles: Cellular Uptake and Cytotoxicity. *Adv. Exp. Med. Biol.* **2014**, *811*, 73−91.

(24) Taylor, J.; Huefner, A.; Li, L.; Wingfield, J.; Mahajan, S. Nanoparticles and intracellular applications of surface-enhanced Raman spectroscopy. *Analyst* **2016**, *141*, 5037−5055.

(25) Kumar, A.; Mohapatra, S.; Fal-Miyar, V.; Cerdeira, A.; García, J. A.; Srikanth, H.; Gass, J.; Kurlyandskaya, G. V. Magnetoimpedance biosensor for Fe3O4 nanoparticle intracellular uptake evaluation. *Appl. Phys. Lett.* **2007**, *91*, 143902.

(26) Wilhelm, C.; Billotey, C.; Roger, J.; Pons, J. N.; Bacri, J.-C.; Gazeau, F. Intracellular Uptake of Anionic Superparamagnetic Nanoparticles as a Function of Their Surface Coating. *Biomaterials* **2003**, *24*, 1001−1011.

(27) Cho, W.-S.; Cho, M.; Jeong, J.; Choi, M.; Cho, H.-Y.; Han, B. S.; Kim, S. H.; Kim, H. O.; Lim, Y. T.; Chung, B. H.; Jeong, J. Acute Toxicity and Pharmacokinetics of 13 Nm-Sized PEG-Coated Gold Nanoparticles. *Toxicol. Appl. Pharmacol.* **2009**, *236*, 16−24.

(28) Huang, M.; Khor, E.; Lim, L.-Y. Uptake and Cytotoxicity of Chitosan Molecules and Nanoparticles: Effects of Molecular Weight and Degree of Deacetylation. *Pharm. Res.* **2004**, *21*, 344−353.

(29) Zhao, M.; Kircher, M. F.; Josephson, L.; Weissleder, R. Differential Conjugation of Tat Peptide to Superparamagnetic Nanoparticles and Its Effect on Cellular Uptake. *Bioconjugate Chem.* **2002**, *13*, 840−844.

(30) Rothbauer, M.; Praisler, I.; Docter, D.; Stauber, R.; Ertl, P.; Technologies, B. Microfluidic Impedimetric Cell Regeneration Assay to Monitor the Enhanced Cytotoxic Effect of Nanomaterial Perfusion. *Biosensors* **2015**, *5*, 736−749.

(31) Lee, R.; Jo, D. H.; Chung, S. J.; Na, H.-K.; Kim, J. H.; Lee, T. G. Real-Time and Label-Free Monitoring of Nanoparticle Cellular Uptake Using Capacitance-Based Assays. *Sci. Rep.* **2016**, *6*, 33668.

(32) Peter, B.; Kurunczi, S.; Patko, D.; Lagzi, I.; Kowalczyk, B.; Rácz, Z.; Grzybowski, B. A.; Horvath, R. Label-Free in Situ Optical Monitoring of the Adsorption of Oppositely Charged Metal Nanoparticles. *Langmuir* **2014**, *30*, 13478−13482.

(33) Peter, B.; Farkas, E.; Forgacs, E.; Saftics, A.; Kovacs, B.; Kurunczi, S.; Szekacs, I.; Csampai, A.; Bosze, S.; Horvath, R. Green Tea Polyphenol Tailors Cell Adhesivity of RGD Displaying Surfaces: Multicomponent Models Monitored Optically. *Sci. Rep.* **2017**, *7*, 42220.

(34) Peter, B.; Nador, J.; Juhasz, K.; Dobos, A.; Korosi, L.; Székács, I.; Patko, D.; Horvath, R. Incubator proof miniaturized Holomonitor toin situmonitor cancer cells exposed to green tea polyphenol and preosteoblast cells adhering on nanostructured titanate surfaces: validity of the measured parameters and their corrections. *J. Biomed. Opt.* **2015**, *20*, 067002.

DOI: 10.1021/acsami.8b01546
ACS Appl. Mater. Interfaces 2018, 10, 26841−26850

(35) Orgovan, N.; Peter, B.; Bősze, S.; Ramsden, J. J.; Szabó, B.; Horvath, R. Dependence of Cancer Cell Adhesion Kinetics on Integrin Ligand Surface Density Measured by a High-Throughput Label-Free Resonant Waveguide Grating Biosensor. *Sci. Rep.* **2014**, *4*, 4034.
(36) Chithrani, B. D.; Chan, W. C. W. Elucidating the Mechanism of Cellular Uptake and Removal of Protein-Coated Gold Nanoparticles of Different Sizes and Shapes. *Nano Lett.* **2007**, *7*, 1542−1550.
(37) Moser, F.; Hildenbrand, G.; Müller, P.; Al Saroori, A.; Biswas, A.; Bach, M.; Wenz, F.; Cremer, C.; Burger, N.; Veldwijk, M. R.; Hausmann, M. Cellular Uptake of Gold Nanoparticles and Their Behavior as Labels for Localization Microscopy. *Biophys. J.* **2016**, *110*, 947−953.
(38) Oh, N.; Park, J. H. Endocytosis and Exocytosis of Nanoparticles in Mammalian Cells. *Int. J. Nanomed.* **2014**, *9*, 51−63.
(39) Xie, X.; Liao, J.; Shao, X.; Li, Q.; Lin, Y. The Effect of Shape on Cellular Uptake of Gold Nanoparticles in the Forms of Stars, Rods, and Triangles. *Sci. Rep.* **2017**, *7*, 3827.
(40) Gunduz, N.; Ceylan, H.; Guler, M. O.; Tekinay, A. B. Intracellular Accumulation of Gold Nanoparticles Leads to Inhibition of Macropinocytosis to Reduce the Endoplasmic Reticulum Stress. *Sci. Rep.* **2017**, *7*, 40493.
(41) Li, Y.; Monteiro-Riviere, N. A. Mechanisms of Cell Uptake, Inflammatory Potential and Protein Corona Effects with Gold Nanoparticles. *Nanomedicine* **2016**, *11*, 3185−3203.
(42) Falagan-Lotsch, P.; Grzincic, E. M.; Murphy, C. J. One Low-Dose Exposure of Gold Nanoparticles Induces Long-Term Changes in Human Cells. *Proc. Natl. Acad. Sci. U.S.A.* **2016**, *113*, 13318−13323.
(43) Shi, L.; Buhler, E.; Boué, F.; Carn, F. How Does the Size of Gold Nanoparticles Depend on Citrate to Gold Ratio in Turkevich Synthesis? Final Answer to a Debated Question. *J. Colloid Interface Sci.* **2017**, *492*, 191−198.
(44) Piella, J.; Bastús, N. G.; Puntes, V. Size-Controlled Synthesis of Sub-10-nanometer Citrate-Stabilized Gold Nanoparticles and Related Optical Properties. *Chem. Mater.* **2016**, *28*, 1066−1075.
(45) Orgovan, N.; Kovacs, B.; Farkas, E.; Szabó, B.; Zaytseva, N.; Fang, Y.; Horvath, R. Bulk and Surface Sensitivity of a Resonant Waveguide Grating Imager. *Appl. Phys. Lett.* **2014**, *104*, 083506.
(46) Allabashi, R.; Stach, W.; de la Escosura-Muñiz, A.; Liste-Calleja, L.; Merkoçi, A. ICP-MS: a powerful technique for quantitative determination of gold nanoparticles without previous dissolving. *J. Nanopart. Res.* **2009**, *11*, 2003−2011.
(47) Shang, L.; Nienhaus, K.; Nienhaus, G. Engineered Nanoparticles Interacting with Cells: Size Matters. *J. Nanobiotechnol.* **2014**, *12*, 5.
(48) Huotari, J.; Helenius, A. Endosome Maturation. *EMBO J.* **2011**, *30*, 3481−3500.
(49) Mayor, S.; Pagano, R. E. Pathways of Clathrin-Independent Endocytosis. *Nat. Rev. Mol. Cell Biol.* **2007**, *8*, 603−612.
(50) Doherty, G. J.; McMahon, H. T. Mechanisms of Endocytosis. *Annu. Rev. Biochem.* **2009**, *78*, 857−902.
(51) Blouin, C. M.; Lamaze, C. Interferon Gamma Receptor: The Beginning of the Journey. *Front. Immunol.* **2013**, *4*, 267.
(52) Aits, S.; Jaattela, M. Lysosomal Cell Death at a Glance. *J. Cell Sci.* **2013**, *126*, 1905−1912.
(53) Hu, Y.-B.; Dammer, E. B.; Ren, R.-J.; Wang, G. The Endosomal-Lysosomal System: From Acidification and Cargo Sorting to Neurodegeneration. *Transl. Neurodegener.* **2015**, *4*, 18.
(54) Maeda, K.; Kato, Y.; Sugiyama, Y. PH-Dependent Receptor/Ligand Dissociation as a Determining Factor for Intracellular Sorting of Ligands for Epidermal Growth Factor Receptors in Rat Hepatocytes. *J. Controlled Release* **2002**, *82*, 71−82.
(55) Horvath, R.; Cottier, K.; Pedersen, H. C.; Ramsden, J. J. Multidepth Screening of Living Cells Using Optical Waveguides. *Biosens. Bioelectron.* **2008**, *24*, 799−804.
(56) Horvath, R.; Pedersen, H. C.; Skivesen, N.; Selmeczi, D.; Larsen, N. B. Monitoring of living cell attachment and spreading using reverse symmetry waveguide sensing. *Appl. Phys. Lett.* **2005**, *86*, 071101.
(57) Skivesen, N.; Horvath, R.; Thinggaard, S.; Larsen, N. B.; Pedersen, H. C. Deep-Probe Metal-Clad Waveguide Biosensors. *Biosens. Bioelectron.* **2007**, *22*, 1282−1288.
(58) Ziblat, R.; Lirtsman, V.; Davidov, D.; Aroeti, B. Infrared Surface Plasmon Resonance: A Novel Tool for Real Time Sensing of Variations in Living Cells. *Biophys. J.* **2006**, *90*, 2592−2599.
(59) Lirtsman, V.; Golosovsky, M.; Davidov, D. Surface plasmon excitation using a Fourier-transform infrared spectrometer: Live cell and bacteria sensing. *Rev. Sci. Instrum.* **2017**, *88*, 103105.

DOI: 10.1021/acsami.8b01546
ACS Appl. Mater. Interfaces 2018, 10, 26841−26850